Magnesium Technology 2012
Edited by: Suveen N. Mathaudhu, Wim H. Sillekens, Neale R. Neelameggham, and Norbert Hort
TMS (The Minerals, Metals & Materials Society), 2012

Magnesium Technology 2012

Poster Session

Session Chair:

Eric A. Nyberg
(Pacific Northwest National Laboratory, USA)

Magnesium Technology 2012
Edited by: Suveen N. Mathaudhu, Wim H. Sillekens, Neale R. Neelameggham, and Norbert Hort
TMS (The Minerals, Metals & Materials Society), 2012

COMBINATION OF COOLING CURVE AND MICRO-CHEMICAL PHASE ANALYSIS OF RAPIDLY QUENCHED MAGNESIUM AM60B ALLOY

P.C. Marchwica[1], A.J. Gesing[2], J.H. Sokolowski[1], C. Blawert[3], J. Jekl[4], R. Berkmortel[4]

[1]University of Windsor
[2]Gesing Consultants Inc.
[3]Helmholtz-Zentrum Geesthacht Zentrum für Material- und Küstenforschung GmbH
[4]Meridian Lightweight Technologies Inc.

Key words: AM60, magnesium, thermal analysis, micro-chemical analysis, rapid quenching

Abstract

Macro test samples of magnesium alloy AM60B were melted and quenched at maximum instantaneous cooling rates ranging from -5°C/s to -500°C/s and the resultant cooling curves were analyzed. Characteristic reactions on these curves corresponding to formation of individual phases were identified with the aid of literature data as well as metallographic and micro-chemical analysis. The results indicate that these phases, their size and location in the microstructure, their chemistry and their relative proportions all change in response to the increase in the cooling rate. These rapid cooling rates are typical of real industrial solidification processes such as die casting. These findings can be used to improve future computer models of casting solidification processes for magnesium and for other alloys.

Introduction

With low density and good mechanical properties, magnesium alloys are increasingly being adopted for use in the automotive industry. As a lightweight structural material they feature excellent ductility, castability and strength and are currently being used for such components as instrument panels, seat frames and steering wheels [1-3]. Many magnesium alloys, such as AM60B, have been developed in order to obtain specific ranges of properties. AM60B, with additions of aluminum and manganese, has good energy-absorption characteristics and ductility [4].

Die casting is the predominant forming method for Mg-based alloys. Large markets for such die-cast alloys include portable consumer electronic housings and automotive/aerospace components. These applications involve use at ambient temperature. Other uses such as engine components expose the alloy to elevated temperature and thus require higher temperature strength and creep resistance. AM60B is a general purpose die-casting alloy containing ~6% Al and >0.3% Mn (wt %). Intended for ambient temperature applications, AM60B is designed for low cost, low density, good castability, and room temperature strength and improved ductility over the industry workhorse AZ91D alloy.

In AM60B, the addition of Al improves the castability by providing the $Mg_{17}Al_{12}$ intermetallic phase, which preserves fluidity during casting until a low temperature (~400°C) eutectic reaction with Mg. Mn has high affinity for impurities such as Fe and Ni (which lead to electrochemical corrosion) and traps them in Al_8Mn_5 intermetallic precipitates. Under thermodynamic equilibrium, these precipitates form in liquid Mg just above its melting point of 650 °C and can be removed with additional melt treatment. Without melt treatment, these precipitates can provide nucleation sites for the solidification of primary αMg grains. Such nucleation promotes reduction of grain size and thus contributes to the improvement in strength and ductility.

Experimental

The Universal Metallurgical Simulator and Analyzer (UMSA) Technology Platform [5] is a desktop thermal analysis system capable of simulating various foundry processes in a quick and cost-effective manner. The basic platform function is heating samples using an induction coil and recording in-situ temperature changes using a thermocouple connected to a data acquisition system. The platform is also applicable to testing other process parameters including cooling/heat treatment cycles and the effects of vacuum/non-atmospheric environments. Recent developments of the platform have focused on improving the quenching capabilities in order to simulate higher cooling rates. While the previous platform was capable of reaching instantaneous cooling rates of around -30°C/s while blowing cold gas at the outer surface of a 18-mm solid cylindrical sample, the latest changes increase simulation capabilities to -500°C/s for macro test samples. The primary reason behind this improvement is the use of hollow test samples that accommodate a central cooling channel and increase the surface-area-to-volume ratio and allow the use of liquid coolants.

The AM60B alloy used in these experiments was provided by Meridian Technologies Inc. in the form of ingots. Nominally pure magnesium was provided in the form of bar stock. Hollow test samples were cut from the raw material with dimensions 12x18x23 mm (IDxODxL) with an additional hole placed within the wall to accommodate the thermocouple. K-type thermocouples (~0.5mm OD) were used in the experiments. Thermocouple calibration was performed using RTD probes. All samples were coated in colloidal graphite and placed in low-thermal-mass stainless steel foil crucibles. The thermocouple was also coated in graphite prior to insertion into the sample. Experimental conditions and process parameters were maintained constant throughout the course of the study. These include holding time, holding temperature, heating rate and atmosphere (argon).

In order to investigate capabilities of the modified UMSA platform, experiments were performed using various combinations of alloy and cooling methods. Each sample in the study was assigned to a particular cooling method and subjected to three repeated heating/cooling cycles. In each cycle, a sample would be heated past its melting point to 750°C and then quenched using its assigned method. Three trials were performed in order to ensure the repeatability of the methods as well as to

maximize thermal contact between the thermocouple and the sample.

Using the modified system, gaseous coolants were found to cool samples at rates up to ~-30°C/s while liquid coolants cooled at rates of up to ~-500°C/s. Images from such rapidly cooled micro-structures are analyzed in this paper. However, rapid cooling induces significant turbulence in liquid coolants, which has a detrimental effect on signal quality. Because of this, thermal analysis in this paper is focused on gas-cooled thermal traces in the -15°C/s to -20°C/s range.

Micro-Chemical and Microstructural Analysis

Tables I shows the alloy compositions as well as the phase compositions and distributions calculated from SEM-EDX measurements. Directional solidification in radial and outward patterns allowed for identification of the sequence of changes in the alloy and phase composition during solidification.

Table I focuses on the AM60B samples solidified at -18°C/s and -280°C/s. Phase composition and distributions calculated in this table are later used in calculations of elemental mass balances for cooling trace analysis. For now, it is significant that at -18°C/s and slower cooling rates we observed equilibrium phases in the sample microstructure: αMg, $Mg_{17}Al_{12}$, Al_8Mn_5 and $MgSi_2$. At a rapid solidification rate of -280°C/s the quantity of intermetallic phases increases by 5 wt% and their composition changes to a metastable structure containing a large excess of Mg.

Table I. Comparison of Phase Compositions and Distributions for Rapidly Solidified AM60B Alloy

		Cooling Rate: -18°C/s to -15°C/s			
	AM60B Alloy	**αMg**	**$Mg_{17}Al_{12}$-αMg Eutectic**	**Al_8Mn_5**	**Mg_2Si**
Phase Distribution	**100.00**	**86.29**	**12.92**	**0.40**	**0.40**
Composition	wt%	wt%	wt%	wt%	wt%
Mg	93.16	97.52	67.10	0.12	63.38
Al	6.26	2.27	32.27	33.58	
Si	0.27	0.07	0.52	0.27	36.62
Mn	0.38	0.14	0.11	60.73	
Fe+Cr+Ni	0.02			5.30	
Total	100	100	100%	100%	100%
		Cooling Rate: -280°C/s			
	AM60B Alloy	**αMg**	**MgAl *IM***	**MgAlMn *IM***	**Mg_2Si**
Phase Distribution	**100.00**	**81.23**	**16.68**	**1.39**	**0.70**
Composition	wt%	wt%	wt%	wt%	wt%
Mg	93.16	97.65	74.26	67.45	63.38
Al	6.26	2.10	25.56	21.12	
Si	0.27	0.01	0.04	0.30	36.62
Mn	0.38	0.24	0.14	11.13	
Fe+Cr+Ni	0.02				
Total	100	100	100	100	100

* *IM* - Intermetallic

Figures 1-4 illustrate the AM60B alloy microstructures and their dependence on the solidification rates. The microstructures are all composed of equiaxed αMg grains, and their grain size is only slightly dependent on the cooling rate up to -240°C/s. Only at -280°C/s is there significant reduction in grain size. This is correlated with the following findings:

1. no Al_8Mn_5 inside αMg grains
2. metastable Mg-rich MgAlMn intermetallics in between αMg grains.

Apparently at very high cooling rates the nucleation of Al_8Mn_5 is suppressed and αMg grains nucleate at more abundant nucleation sites, probably small oxide inclusions.

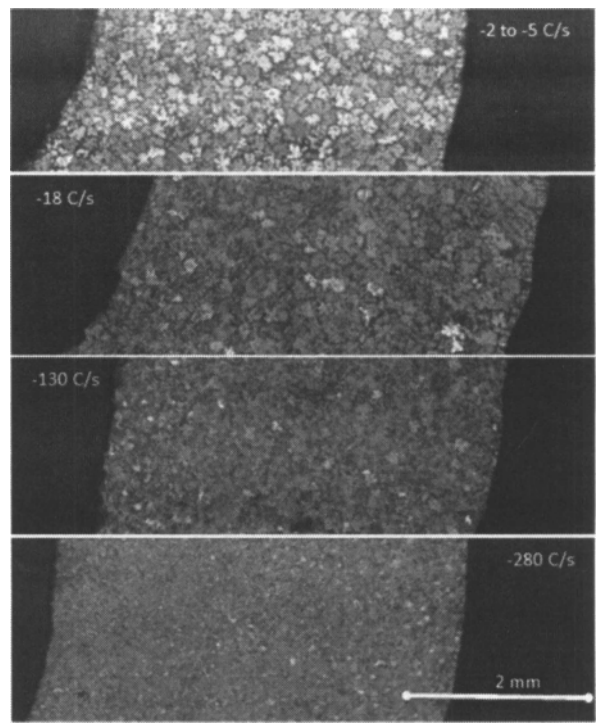

Figure 1. Alloy AM60B – Dependence of grain size on solidification rate. At >-20°C/s, the grain structure (equiaxed) and direction (radially outward) are not noticeably affected by solidification rate. At more rapid rates, grain size decreases and there is a slight size gradient in the solidification direction with grains growing larger later.

The peak cooling rate is recorded at the start of solidification. As the cooling proceeds, the baseline cooling rate slows down. Figure 2 illustrates how this affects the grain structure in a directionally solidified sample starting at -280°C/s. There is noticeable grain coarsening between the start and end regions of the sample (at inner and outer walls).

Figure 3 illustrates how interdendritic melt solidification at the end differs with the cooling rate. At slow cooling rates, equilibrium αMg-$Mg_{17}Al_{12}$ eutectic forms as a spongy two-phase structure. In the -240°C/s and -280°C/s samples, the equilibrium phases are replaced by the metastable Mg-rich intermetallics, Mg_xAl_y and $Mg_xAl_yMn_z$.

Figure 4 illustrates that as the cooling rate increases αMg solidification becomes more dendritic and the equiaxed grains become equally equiaxed dendritic rosettes expanding radially out from the central nucleation site.

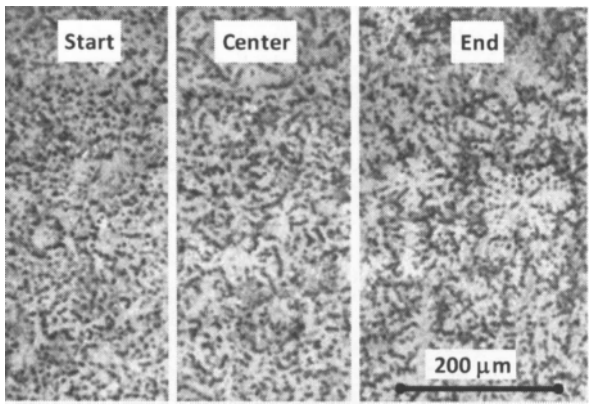

Figure 2. Alloy AM60B – Comparison of grain size and morphology in start, center and end regions for a sample solidified at -280°C/s. Images were taken from a polished and etched section accentuating the grain boundaries and intermetallics which are found both inside and between αMg grains.

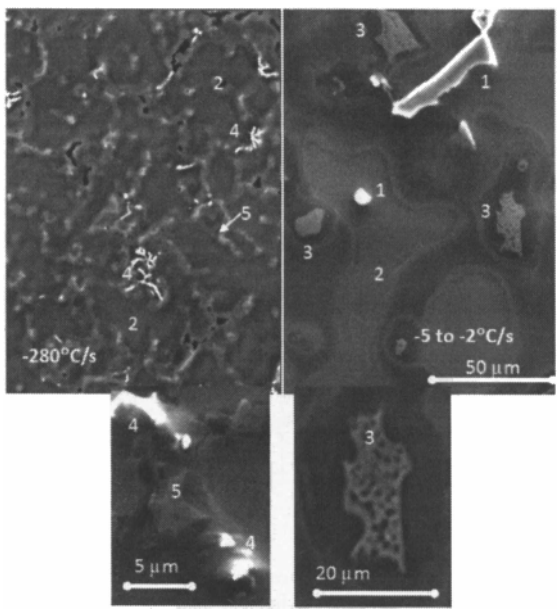

Figure 3. BSE + SE images of AM60B alloy solidified at -280°C/s (left) and -5 to -2 °C/s (right) showing changes in the micro-structure with cooling rate. At -5 to -2 °C/s we see: 1. blocky Al_8Mn_5 inside, 2. αMg grains and, 3. $\beta Mg_{17}Al_{12}$–αMg eutectic in-between, while at -280°C/s there is 4. dendritic $Mg_xAl_yMn_z$ and 5. single phase Mg_xAl_y in between αMg grains.

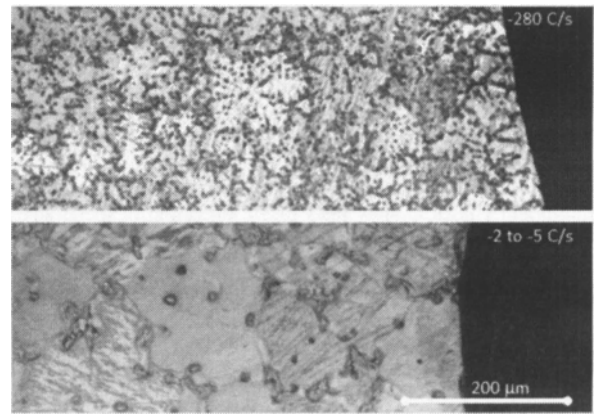

Figure 4. Alloy AM60B – Comparison of grain morphology in the start region between samples solidified at -280°C/s and at -2°C/s to -5°C/s. Enhanced tendency for dendritic growth is shown at higher solidification rates. Grains nucleate at solid particles and grow outward in all directions regardless of the direction of heat extraction. (Sample is cooled from the center.)

The AM60B alloy microstructures tell a story. There is a smaller but still significant variation in alloy microstructures attributable to the nearly two orders of magnitude change in the solidification rates.

In all cases the structure is dominated by a nearly equiaxed structure of pretty uniformly sized αMg grains. At slow cooling rates one tends to find small dendritic Al_8Mn_5 structures inside the αMg grains. There are also occasional small equiaxed Mg_2Si crystals located near the grain boundaries but still typically surrounded with αMg phase. Between the αMg grains there is spongy eutectic structure of $\beta Mg_{17}Al_{12}$ with αMg inclusions. At rapid solidification rates between the αMg grains, there is a layer of Mg-rich MgAl intermetallic. The grain sizes decreased slightly and the equiaxed αMg structures changed from grains to small dendritic rosettes growing out from central Al_8Mn_5 intermetallics. At the fastest cooling rate of nearly -300°C/s, there was significant further reduction in the αMg grain size, and the Al_8Mn_5 intermetallics were replaced by Mg-rich MgAlMn crystals forming in the MgAl phase found at the αMg grain boundaries.

The sequence that would account for these observations at all but the fastest cooling rates involves starting with homogeneous nucleation of Al_8Mn_5, which starts growing and exhausts the supply of the Mn alloying element and reduces the concentration of other transition elements in the melt. Each Al_8Mn_5 structure appears to be an effective nucleation site for the αMg grains. As αMg grains grow they concentrate Al and Si in the melt. Eventually, at sufficient Si concentration, Mg_2Si co-precipitates with the αMg. The equilibrium phase diagram predicts formation of αMg- $\beta Mg_{17}Al_{12}$ eutectic structure to finish the solidification sequence, which we observed experimentally at slow cooling rates. At rapid solidification rates the last phase to solidify was single-phase Mg-rich MgAl intermetallic in between the αMg grains and dendritic rosettes. Significantly this correlated to a loss of the exothermic peak from the cooling curve that we associated at the slow cooling curves with $\beta Mg_{17}Al_{12}$-αMg eutectic formation.

At the fastest cooling rate the undercooling is sufficient to delay Al_8Mn_5 nucleation and permit homogeneous nucleation of αMg

throughout the melt volume, resulting in the observed extra fine grain size. Mn concentrates in the residual melt and finally comes out near the end as MgAlMn crystal in MgAl phase found between the αMg grains.
In the AM60B alloy the microstructure changed quite significantly with the increase in the solidification rate. This microstructural change is associated in the change in both the sequence of phase formation and in the shift from the formation of equilibrium phases at slow rates to the formation of metastable phases during rapid cooling.

Cooling Curve Analysis

The cooling curve is derived from the time-temperature record of the sample being cycled through repeated melting and solidification cycles. We calculate the slope of a linear fit to several adjacent data points to smooth and differentiate the temperature data with respect to time. The cooling rate becomes less negative as the sample temperature drops, reducing the temperature difference between the sample and the coolant. The area of the peaks superposed on this sloped baseline represents the enthalpy of solidification of the various solid phases crystalizing out of the melt. To calculate the peak areas one must first calculate the portion of the baseline in the semi-solid region.

Baseline Determination

For the magnesium parent metal, the heat capacities of liquid and solid are different, which results in a shift in the baseline between the fully solid and fully liquid regions. At any temperature:

$$B_s/B_l = c_{pl}/c_{ps} \quad (1)$$

where B_s and B_l are baselines determined in liquid and solid respectively, and c_{pl} and c_{ps} are heat capacities of the liquid and solid. Further, in the semi-solid region the baseline value for the semisolid mixture, B, can be calculated from the respective weight fractions of liquid and solid, f_l and f_s as follows:

$$1/B = (1-f_s)/B_l + f_s/B_s \quad (2)$$

Fraction solid at any time is estimated from the fraction of the total thermal solidification peak area that was integrated to that time. Since the peak area depends on the baseline, an iterative solution is required. The procedure is found to converge to a solution after a few iterations. The problem is simplified by ignoring the contribution of alloying elements to the baseline value. Figure 9 shows an example of the cooling curve as a function of temperature with the calculated baseline that accounts for the liquid and solid contributions in the semi-solid region. At the solidus (end of solidification) temperature the position of the B_l is calculated from the measured B_s value. This point is linearly interpolated to the measured B_l curve at the liquidus (start of solidification) temperature. The B_s curve between the liquidus and the solidus is then calculated from the B_l interpolated values according to equation 1. The baseline B for the semisolid mix is then calculated from B_s and B_l by iterative solution of Equation 2.

Enthalpy Calibration

The area of the baseline subtracted peak plotted against solidification time is proportional to the enthalpy of formation of the solid phase. The proportionality factor was determined by measuring the peak area for commercially pure Mg which has a latent heat of solidification of 8.48 KJ/mole reported for pure Mg by NIST at the melting point. The calibration is complicated by two facts. First, the measured area of the solidification peak depends on the cooling rate. The area, increases as the cooling rate goes more negative. Second, the enthalpy of solidification decreases as solidification temperature decreases. This decrease is significant for alloys with a wide solidification temperature range. The calibration measurements in commercially pure Mg spanned a range of -2°C/s to -20°C/s for a baseline value in during actual solidification. Linear interpolation fit to this data was used to calculate the conversion factor from the area measured in degrees centigrade to energy measured in joules:

$$C2J = \Delta H_m(T)/AP(dT/dt) \quad (3)$$

Here $\Delta H_m(T)$ is the latent heat of solidification of Mg at temperature T, and AP(dT/dt) is the measured area of the dT/dt peak with baseline subtracted and integrated with respect to time, at a specific baseline cooling rate. Individual C2J calibration factors were calculated for each data point and applied to the baseline subtracted dT/dt peak profile data before area integration. This allowed us to account for variation of the calibration factor with both temperature and the baseline cooling rate during the solidification event.
Figures 5, 6 and 7 show examples of the cooling curve baseline subtraction and calibration results for the alloy AM60B.

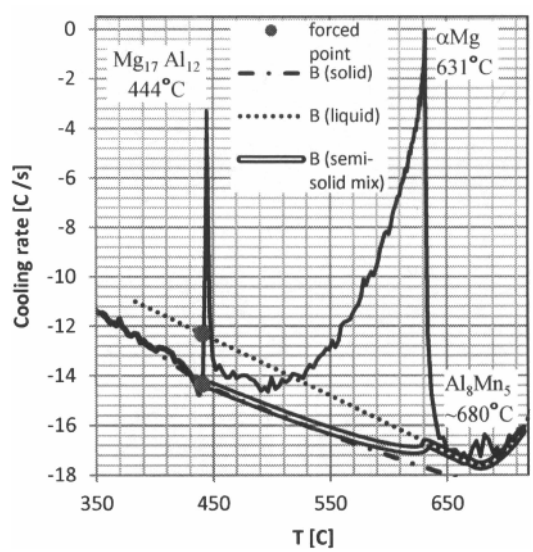

Figure 5. AM60B alloy cooling curve with calculated baseline. Liquid baseline is extrapolated linearly to a point located at solidus temperature and a value given by Equation 1. The solid baseline is extrapolated to the liquidus temperature based on Equation 1 and the interpolated value of liquid baseline. Semi-solid mix baseline is calculated from the solid and liquid baselines according to Equation 2.

The correlation between the cooling curve peaks, the phases observed in the microstructure and their identification is based on the phase quantity and location in the structure and the literature results on phase thermochemical and crystallographic properties and the alloy equilibrium phase diagram [7].

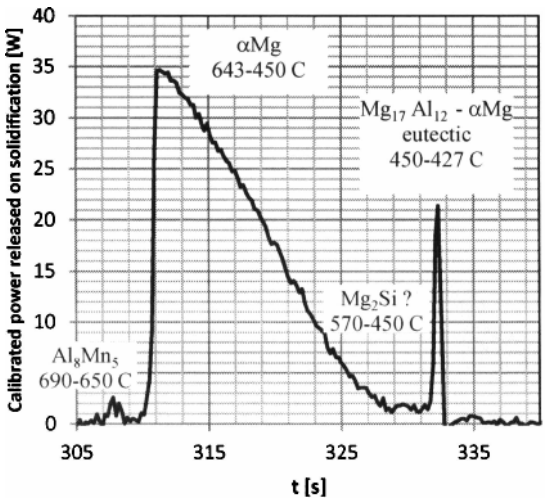

Figure 6. Calibrated values of the power released during solidification of a 5.7-g AM60B alloy sample at -18°C/s to -15°C/s. Integration of the individual peak areas yields experimental values for enthalpy of formation.

Phase Formation

The phase distribution information calculated from the microstructural and micro-chemical observations is combined with the evolution of fraction solid of each individual phase during the solidification event to generate a plot demonstrating the formation of the constituent solid phases and consumption of the melt as a function of the temperature. An example of such a plot for AM60B solidified at -18°C/s to -15°C/s is shown in Figure 7.

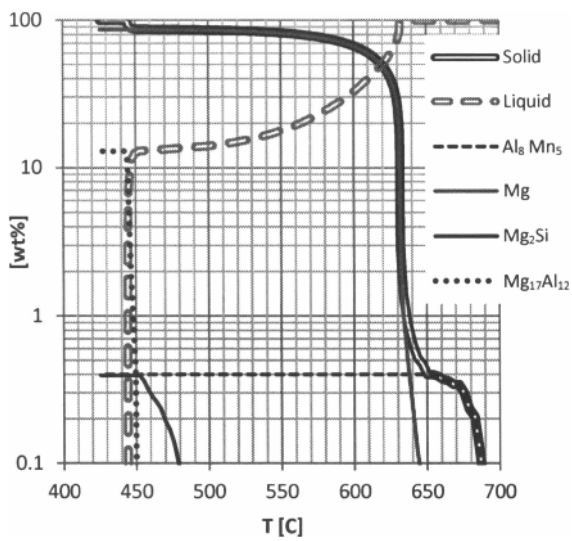

Figure 7. AM60B alloy phase evolution during solidification at -18°C/s to -14°C/s. The solid forms as 0.3% of Al_8Mn_5 between 687°C and 650°C; 85% as αMg between 643°C and 450°C and finally as 12% of $Mg_{17}Al_{12}$ -- αMg eutectic between 450°C and 428°C.

Table II: Enthalpy of formation of intermetallic phases from AM60B melt solidifying at -18°C/s

	Alloy latent heat	αMg	$Mg_{17}Al_{12}$- αMg eutectic	Al_8Mn_5	Mg_2Si
ΔH_f [J/g]	-289	-317	-79	-535	-605
T_{start} [C]	697	647	452	697	491
T_{max} [C]	632	632	445	683	482
T_{end} [C]	441	452	441	654	452

Table II summarises the key cooling curve information from solidification of AM60B at -18°C/s. Integration of peaks in Figure 10 associated with individual phases provides the information for this table. As expected the latent heat of solidification of the alloy is lower than that for pure Mg. Forming αMg in this alloy yields -317 J/g as compared with -348 J/g for formation of the same phase from pure Mg melt. Formation of the eutectic yields relatively little heat, whereas the formation of Al_8Mn_5 and Mg_2Si are highly exothermic.

Solidification Path: Evolution of Melt Composition

Information illustrated in Figure 7 combined with the composition of the individual phases allow the calculation of the residual liquid composition during the solidification event. Knowledge of such solidification path is key to understanding the phase formation during solidification. The solidification path is plotted as concentration of the individual alloying elements as a function of temperature in Figure 8.

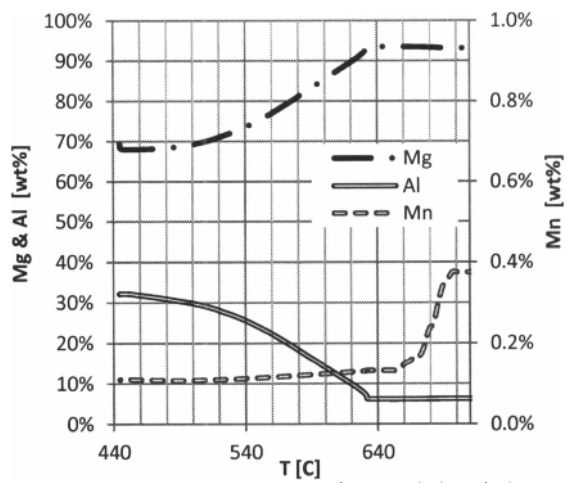

Figure 8. AM60B alloy melt composition variation during solidification at -18°C/s to -14°C/s

At very rapid cooling rates interpretation of the cooling curves becomes more difficult. Total solidification time reduces to a few seconds. During that time there is the initial transient of introducing the coolant to the molten sample and setting up a stable boundary layer and heat transfer coefficient between the coolant and the sample. When liquid coolant is used, it is common to observe vapor or air bubbles exiting the cooling tube. This suggests that an insulating gas film may form on the hot cooling tube surface and impede the cooling process. This can lead to

irreproducible, apparent thermal peaks that have nothing to do with the enthalpy of alloy solidification. In this paper we limited the reported cooling curve data to >-25°C/s, which is a rate that we can consistently reach using compressed gas coolant. This eliminates the possibility of insulating vapor film formation on the cooling tube surface.

Further, there is an implicit assumption in the analysis that the sample is isothermal. This is valid at slow cooling rates because of very high thermal conductivity of the metal sample. However, as cooling rates reach hundreds of degrees per second, the heat flux required to achieve such a rate also requires a temperature gradient in the sample. The effect of the gradient causes the apparent exotherm to start at a higher temperature than recorded by the centrally located thermocouple and continues to a lower temperature after solidification is complete at the thermocouple location. This effect is reproducible and we calibrated it out for enthalpy measurements by performing the calibration measurements on pure Mg over the cooling rate range spanning the rates of interest for gas cooling. Extrapolation of these calibration values to more rapid liquid coolant rates was not successful. The temperature gradient in the sample spreads the exotherm over a range of temperatures. This can cause small and overlapping exotherms to be smeared out and lost in the baseline noise.

Conclusions and Future Work

The UMSA technology platform has been modified to enable solidification of alloy melts at cooling rates up to -500°C/s.

A combination of cooling curve analysis with microstructural and micro-chemical results yields a wealth of information on the phases formed, sequence of events, the enthalpies of formation of component phases and evolution of residual melt composition during solidification.

Reliable and reproducible cooling curves were obtained with sufficient detail to resolve the component phase contributions at cooling rates up to -20°C/s for AM60B alloy.

At very rapid solidification rates detail is lost from the cooling traces due to a combination of actual change in the type and quantity of phase formed, and as well to experimental limitations. Future work will focus on eliminating the experimental limitations and extending the cooling rate range over which reliable, quantifiable results can be obtained.

Acknowledgements

This research was partially funded by AUTO21, a member of the Networks of Centres of Excellence of Canada program. NSERC Discovery Grant also partially funded this research. The GCI contribution was partially funded by the Canadian SR&ED program. Assistance from Sharon Lackie and Andy Jenner in the analysis and machining of samples is also gratefully acknowledged.

References

1. A. Kiełbus, "Microstructure of AE44 magnesium alloy before and after hot-chamber die casting," *Journal of Achievements in Materials and Manufacturing Engineering*, Vol. 20(1-2), (2007), 459-462.

2. T. Rzychoń, A. Kiełbus, J. Cwajna, and J. Mizera, "Microstructural stability and creep properties of die casting Mg–4Al-4RE magnesium alloy," *Materials Characterization*, Vol. 60, (2009), 1107-1113.

3. J.P. Weiler, J.T. Wood, R.J. Klassen, R. Berkmortel, and G. Wang, "Variability of skin thickness in an AM60B magnesium alloy die-casting," *Materials Science and Engineering*, Vol. 419, (2006), 297-305.

4. W. Huanga, B. Hou, Y. Pang, and Z. Zhou, "Fretting wear behavior of AZ91D and AM60B magnesium alloys," *Wear*, Vol. 260, (2006), 1173-1178.

5. A.E.W. Jarfors, K.-U. Kainer, Ming-Jen Tan, and J. Yong, "Recent Developments in the Manufacturing of Components from Aluminium-, Magnesium- and Titanium-Based Alloys," *COSMOS*, 5(1), 2009), 23-58.

6. A.J. Gesing, N.D. Reade, J.H. Sokolowski, and C. Blawert, "Solidification Behavior of Recyclable Mg Alloys - AZ91 and AZC1231," *Magnesium Technology 2009*, (San Francisco, CA: The Minerals, Metals & Materials Society, 2009), 117-128.

7. D. Mirković and R. Schmid-Fetzer, "Solidification Curves for Commercial Mg Alloys Determined from Differential Scanning Calorimetry with Improved Heat-Transfer Modeling," *Metallurgical and Materials Transactions A*, 38A (October 2007), 2575-2592.